JACS
JOURNAL OF THE AMERICAN CHEMICAL SOCIETY

Article

pubs.acs.org/JACS

Thermally Highly Stable Amorphous Zinc Phosphate Intermediates during the Formation of Zinc Phosphate Hydrate

Sven Bach,[†,§] Vinicius R. Celinski,[‡] Michael Dietzsch,[†] Martin Panthöfer,[†] Ralf Bienert,[∥] Franziska Emmerling,[∥] Jörn Schmedt auf der Günne,[‡] and Wolfgang Tremel*[,†]

[†]Institute of Inorganic Chemistry and Analytical Chemistry, Johannes Gutenberg University Mainz, Duesbergweg 10-14, D-55128 Mainz, Germany

[§]Graduate School, Materials Science in Mainz, Staudinger Weg 9, D-55128 Mainz, Germany

[‡]Inorganic Materials Chemistry, University of Siegen, Adolf-Reichwein-Straße 2, D-57068 Siegen, Germany

[∥]Federal Institute for Materials Research and Testing, Richard-Willstätter-Straße 11, D-12489 Berlin, Germany

Supporting Information

ABSTRACT: The mechanisms by which amorphous intermediates transform into crystalline materials are still poorly understood. Here we attempt to illuminate the formation of an amorphous precursor by investigating the crystallization process of zinc phosphate hydrate. This work shows that amorphous zinc phosphate (AZP) nanoparticles precipitate from aqueous solutions prior to the crystalline hopeite phase at low concentrations and in the absence of additives at room temperature. AZP nanoparticles are thermally stable against crystallization even at 400 °C (resulting in a high temperature AZP), but they crystallize rapidly in the presence of water if the reaction is not interrupted. X-ray powder diffraction with high-energy synchrotron radiation, scanning and transmission electron microscopy, selected area electron diffraction, and small-angle X-ray scattering showed the particle size (≈20 nm) and confirmed the noncrystallinity of the nanoparticle intermediates. Energy dispersive X-ray, infrared, and Raman spectroscopy, inductively coupled plasma mass spectrometry, and optical emission spectrometry as well as thermal analysis were used for further compositional characterization of the as synthesized nanomaterial. ^{1}H solid-state NMR allowed the quantification of the hydrogen content, while an analysis of ^{31}P{^{1}H} C rotational echo double resonance spectra permitted a dynamic and structural analysis of the crystallization pathway to hopeite.

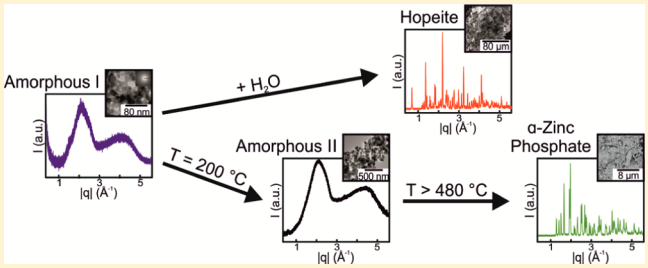

1. INTRODUCTION

Precipitation and crystallization are key methods for the synthesis of high-value organic and inorganic products where purity, size distribution, and crystal shape are important.[1,2] There is a profound interest to direct these processes to get hold on stabilization of certain phases or polymorphs by controlling nucleation, growth, Ostwald ripening, and aggregation which are in turn governed by a proper choice of conditions, e.g., with the help of additives, or by regulating the solubility−precipitation equilibria.[3,4] The selective crystallization of a certain polymorph and its stabilization is a challenging task because the thermodynamic and kinetic factors affecting crystallization processes are difficult to control. In the past decade, the early stages of phase formation, i.e., nucleation and early growth as well as the question, to what extent metastable states can be maintained by controlling crystallization mechanisms and kinetics, have received much attention.

Many of these studies have been performed on calcium carbonate.[5] This choice is based both on relevance (i.e., industrial application, scale formation, or biomineral formation) and on the time scale that is needed for crystallization. Amorphous calcium carbonate (ACC) is a reactive transient intermediate and transforms into one of the crystalline forms in the presence of water or when heated. It can form in both biological and abiotic environments. In nature, ACC is a precursor to the crystalline polymorphs calcite and aragonite, e.g., in various shells and spicules.[6−8] Synthetic ACC is formed from highly supersaturated solutions or polymer-stabilized liquid precursors at or below room temperature.[9−15] Soluble clusters—similar in size to the structural coherence length of ACC—have been observed in solution prior to the nucleation of calcium carbonate. Based on equilibrium thermodynamics, Gebauer et al.[16] demonstrated the formation of stable ∼2 nm clusters prior to nucleation. Pouget et al.[17] observed the initial formation of prenucleation clusters using cryo-TEM. Upon aggregation and in the presence of proteins, these clusters lead to the formation of ACC nanoparticles with diameters of ∼30 nm.[18] These observations indicate a crystallization pathway for calcium carbonate through stable prenucleation clusters[19−21] as opposed to the picture provided by classical nucleation theory.[22]

Received: October 9, 2014
Published: January 20, 2015

ACS Publications © 2015 American Chemical Society

DOI: 10.1021/ja5103663
J. Am. Chem. Soc. 2015, 137, 2285−2294

In order to test the viability and the limits of the classical crystallization pathway, new model systems for crystallization are needed. Moderate charge densities of cations like Ca^{2+} or Zn^{2+} may be a promising guideline to identify candidates for nonclassical crystallization pathways due to their possibility to bind water reversibly. Apatite[23] and $CaSO_4$[24,25] are well-documented cases besides $CaCO_3$. Similarly, the charge density of Zn^{2+} indicates the possibility to form a variety of hydrated polymorphs in compounds like zinc sulfate[2] or zinc phosphate.[26−31]

In nature, zinc phosphate occurs as tetrahydrate in two polymorphs, orthorhombic hopeite and triclinic parahopeite. Hopeite arises in three different modifications (α-, β-, and γ-hopeite) that differ only in the order of crystal water molecules.[32−38] Zinc hydrogen phosphate trihydrate (ZHPT) forms by slightly changing the synthesis conditions used to obtain α-hopeite.[31] Stepwise dehydration first leads to the formation of zinc phosphate dihydrate and later to anhydrous zinc phosphates.[31,39]

Crystallization of zinc phosphate in the presence of organic templates[40,41] leads to the formation of microporous zinc phosphates with zeolite-like topologies,[40−44] although the formation mechanism of these open framework structures is still poorly understood. Furthermore, zinc phosphates have important technical applications such as cements, filling material in plastics, as corrosion inhibitors, and for the prosthetic and conservative therapy of bones and teeth.[45−49] Hopeite ($Zn_3(PO_4)_2 \times 4\ H_2O$) and phosphophyllite ($Zn_2Fe(PO_4)_2 \times 4\ H_2O$) are important phases used in the formation of corrosion resistant coatings on steel[50−56] and as a host lattice for fluorescent materials or long-lasting phosphors.[57−59]

Inorganic nanoparticles tend to form polymorphs different from the thermodynamically stable one for small particle sizes, although hydrated and/or dehydrated amorphous phases are metastable with respect to their crystalline counterparts.[60] Calorimetric measurements by Navrotsky and co-workers[61] have shown the competition between lattice and surface energy to be responsible for this polymorph change,[62,63] and it could be shown that the stability regime of metastable polymorphs can be extended significantly for small particle sizes.

Therefore, the formation of amorphous zinc phosphate as a transient precursor during the early stages of crystallization may be preferred for nanoparticles, but so far there are only few reports on zinc phosphate nanoparticles. $Zn_3(PO_4) \times 2\ H_2O$ nanoparticles have been synthesized at room temperature by grinding sodium phosphate dodecahydrate and zinc sulfate heptahydrate in the presence of a nonionic surfactant.[64] In addition, $Zn_3(PO_4)_2$ nanoparticles have been prepared from microemulsions.[65] Amorphous zinc phosphate hydrate nanoparticles have been obtained in anhydrous media via the polyol method,[66] and solid-state NMR proved an important analytical tool of characterization for both amorphous and crystalline nanoparticles[66−70] because of its ability to probe local atomic environments and water content of the samples.

We have prepared AZP hydrate nanoparticles with diameters of ≈20 nm by direct precipitation from aqueous solutions at low concentrations and short reaction times. The AZP nanoparticles exhibit an impressive thermal stability even at 400 °C, but they rapidly crystallize in the presence of water. Their noncrystallinity was demonstrated by powder X-ray diffraction (PXRD) with high-energy synchrotron radiation, small-angle X-ray scattering (SAXS), vibrational (IR, Raman) spectroscopy, scanning and transmission electron microscopy (SEM, TEM) in combination with selected area electron diffraction (SAED). Differential scanning calorimetry/thermogravimetry (DSC/TG), inductively coupled plasma mass spectrometry (ICP-MS) and optical emission spectrometry (ICP-OES), and energy dispersive X-ray spectroscopy (EDX) provided analytical information concerning the elemental composition and ^{1}H MAS NMR spectra allowed the quantification of the hydrogen content, while an analysis of $^{31}P\{^1H\}$ C rotational echo double resonance (REDOR) spectra permitted a dynamic and structural analysis of the crystallization pathway to hopeite.

2. EXPERIMENTAL SECTION

2.1. Synthesis. AZP nanoparticles were prepared by direct precipitation from solution. $Zn(NO_3)_2 \times 2\ H_2O$ (>98%, Sigma-Aldrich) (10 mL) (solution 1), and Na_3PO_4 (>96%, Sigma-Aldrich) were dissolved in deionized water (10 mL) (solution 2, both at ambient temperature), and solution 1 was stirred with 400 rpm in a beaker, while solution 2 was added. To instantly separate the precipitated solids from solution, the mixture was centrifuged (9000 rpm, 5 min) immediately. Subsequently, the solid was resuspended in and centrifuged from acetone p.A. (≥99.5%, Sigma-Aldrich) three times to remove adsorbed water. The solid was dried at room temperature under dynamic vacuum ($p = 3 \times 10^{-3}$ mbar) for 2 days.

2.2. Characterization. SEM analysis was performed with a Zeiss Gemini Supra 40 microscope (samples sputtered with carbon, acceleration voltage 15 kV, working distance 2.8 mm). TEM analysis was carried out on a Philips EM-420 microscope (acceleration voltage 120 kV). Samples for TEM snapshots were prepared by taking aliquots of the sample from solution after mixing the source solutions and before centrifugation. Samples were prepared on a carbon-coated copper grid and vacuum-dried at room temperature. SAXS measurements were performed with a SAXSess device of Anton Paar using monochromated CuKα radiation and a CCD camera.

EDX analysis was performed with a Bruker Quantax 400 device mounted on the Zeiss microscope. Fourier-transform infrared (FT-IR) spectra were measured with a Bruker Alpha-P FT-IR spectrometer with platinum ATR. The spectra were recorded 24 times with a resolution of 4 cm^{-1}. Raman spectra were recorded with a Horiba Jobin Yvon spectrophotometer equipped with a Nd:YAG laser for the region between 150 and 1500 cm^{-1}. The scan rate was 2700 cm^{-1} min^{-1}.

For ICP-MS measurements, a precisely weighed amount of AZP nanoparticles was solubilized with 5 mL of sub-boiled conc. HNO_3 in a Teflon vessel by microwave digestion. The digestion solution was filled up to 100 mL with deionized water and diluted subsequently 1:1000 with 3.3% HNO_3. Blanc values for 5 mL conc. HNO_3 filled up to 100 mL with deionized water were subtracted. The measurements were performed on an ICP-sector field-MS device, Thermo element 2 (Thermo Scientific, Bremen, Germany) (medium resolution R = 4500). The sample was conducted to the ICP-SF-MS by a PFA nebulizer (gas flow: 1.22 L min^{-1}, cooling gas: 16 L min^{-1}) through a Peltier-cooled PFA-cyclone-spray chamber PC^3 (4 °C) (Elemental Scientific Inc., Omaha, NE, U.S.A.). The samples were analyzed 10 times for 70 s with a dwell time of 10 s. Quantification was performed with external calibration (standard solutions prepared with 3.3% HNO_3).

ICP-OES was performed using a PerkinElmer Optima 8300 (power 1300 W). Therefore, the same diluted solutions were used as for the ICP-MS measurements. Samples were conducted to the ICP-OES by a MiraMist nebulizer (Burgener Canada) (gas flow: 0.55 L min^{-1}, auxiliary gas flow: 0.2 L min^{-1}). Samples were ionized trough a plasma flow of 13 L min^{-1}. It was measured at wavelengths of 206.200 (Zn) and 178.223 nm (P), each time for 10 s.

DSC and TG analysis were carried out on a Netzsch STA 449 F3 Jupiter. Samples were deposited in an ALOX crucible and heated from 20 to 800 °C under argon with a heating rate of 1 K min^{-1} and a flow rate of 10 mL min^{-1}.

DOI: 10.1021/ja5103663
J. Am. Chem. Soc. 2015, 137, 2285−2294

Solid-state NMR experiments were on a Bruker Avance III-500 spectrometer equipped with a 1.3 and a 2.5 mm double resonance MAS probe at a ^{1}H frequency of 500.13 MHz (magnetic field 11.7 T) and on a Bruker Avance II spectrometer equipped with a 4 mm homemade double resonance MAS probe at a ^{1}H frequency of 200.0 MHz (magnetic field 4.74 T). Saturation combs were used before all repetition delays. The chemical shifts of ^{1}H were reported using the δ scale, relatively to 1% tetramethylsilane (TMS) in $CDCl_3$. The ^{1}H resonance of 1% TMS in $CDCl_3$ was also used as an external secondary reference for the ^{31}P resonance of 85% H_3PO_4 using the Ξ-values for ^{31}P as reported by the IUPAC.[71] The $^{31}P\{^{1}H\}$ MAS NMR spectrum was obtained at a sample spinning frequency ν_r of 40 kHz with repetition delays of 128 s and 16 transients. The ^{1}H MAS NMR spectrum was obtained at a sample spinning frequency ν_r of 40 kHz with a repetition delay of 1 s and 128 transients. Proton decoupling was implemented using two-pulse phase-modulation (TPPM) decoupling with a nutation frequency of 100 kHz. The channels used in the C-REDOR[69,70] experiments are denoted as S{I}, where S refers to the observed nucleus and I to the recoupled one. The $^{31}P\{^{1}H\}$ C-REDOR experiment was performed at a sample spinning frequency ν_r of 40 kHz with a recycle delay set to 27 s, accumulated 32 transients/FID and was implemented using TPPM decoupling with a nutation frequency of 16 kHz. The crystal structure of hopeite used for the calculation of C-REDOR curves was taken from ref 72.

XRD measurements of crystalline samples were conducted with a Bruker AXS D8 Discover equipped with a Highstar Detector and using monochromated CuKα (1.5418 Å) radiation.

High-resolution synchrotron powder diffraction data of AZP were collected using beamline 11-BM at the Advanced Photon Source (APS), Argonne National Laborator, using an average wavelength of 0.413664 Å. Discrete detectors covering an angular range from −6 to 16° 2Θ were scanned over a 34° 2Θ range, with data points collected every 0.001° 2Θ and scan speed of 0.01°/s.

The 11-BM instrument uses X-ray optics with two platinum-striped mirrors and a double-crystal Si(111) monochromator, where the second crystal has an adjustable sagittal bend.[73] Ion chambers monitor incident flux. A vertical Huber 480 goniometer, equipped with a Heidenhain encoder, positions an analyzer system comprised of 12 perfect Si(111) analyzers and 12 Oxford-Danfysik $LaCl_3$ scintillators, with a spacing of 2° 2Θ.[74] Analyzer orientation can be adjusted individually on two axes. A three-axes translation stage holds the sample mounting and allows it to be spun, typically at ∼5400 rpm (90 Hz). A Mitsubishi robotic arm is used to mount and dismount samples on the diffractometer. An Oxford Cryosystems Cryo-stream Plus device allows sample temperatures to be controlled over the range 80−500 K when the robot is used.

The diffractometer was controlled via EPICS.[75] Data were collected while continually scanning the diffractometer 2Θ arm. A mixture of NIST standard reference materials Si (SRM 640c) and Al_2O_3 (SRM 676) is used to calibrate the instrument, where the Si lattice constant determines the wavelength for each detector. Corrections are applied for detector sensitivity, 2Θ offset, small differences in wavelength between detectors, and the source intensity, as noted by the ion chamber before merging the data into a single set of intensities evenly spaced in 2Θ.

3. RESULTS AND DISCUSSION

3.1. Synthesis. Our initial attempts to synthesize AZP followed the approach of Faatz et al.[10] for the synthesis of ACC using the hydrolysis of a trialkyl phosphate in aqueous solution because ester hydrolysis proceeds on a time scale ideally suited for monitoring the reaction *in situ*. However, when trialkyl phosphates were hydrolyzed at a fixed pH in an aqueous solution of zinc chloride, ZnO (zincite) rather than AZP precipitated because at pH 11 (required for the ester hydrolysis) the solubility product (3.0×10^{-17} mol^{-3})[76] of $Zn(OH)_2$ was reached. $Zn(OH)_2$ quickly transforms in a follow-up reaction to ZnO.

Therefore, we attempted the precipitation of AZP by fast mixing of aqueous solutions of $Zn(NO_3)_2 \times 6\ H_2O$ and Na_3PO_4 (final pH = 6.86). The precipitates were separated by centrifugation, resuspended in acetone, centrifuged, and finally dried to remove physisorbed water. According to Ostwald's rule,[2,77,78] the least stable (amorphous) polymorph should be formed first and transform subsequently to the thermodynamically stable hopeite (solubility product: 2.51×10^{-35} $mol^5\ L^{-5}$).[79] The thermodynamic driving force for the crystallization from solution is given by the difference in the chemical potential of zinc phosphate in a supersaturated solution and in the crystal. The degree of supersaturation is a key variable in any precipitation that is governed by the rate of nucleation and growth. Short reaction times and high supersaturation are expected to favor the formation of AZP. The formation of amorphous compounds at high supersaturations is not in conflict with a classical kinetic crystallization pathway,[77] but the classical model of equilibrium states appears to have limitations.[80] To understand the formation of amorphous zinc phosphate and its transformation in solution with time, the precipitation experiments were conducted at time intervals ranging from 5 s to 1 day with different starting concentrations (ranging from 10 to 300 mM) of the zinc nitrate and sodium phosphate solutions.

However, crystalline hopeite was obtained even for the shortest reaction times from concentrated solutions (300 mM Zn^{2+} and 200 mM PO_4^{3-}), which might be due to a fast amorphous → crystalline phase transformation. Therefore, the precipitation was performed from dilute solutions (15 mM Zn^{2+} and 10 mM PO_4^{3-}). For short reaction times (5 s) pure AZP was obtained as demonstrated by the absence of reflections in the X-ray diffractogram (Figure 1A), whereas longer reaction times (>4 min) lead to the formation of crystalline hopeite (Figure 1B).

3.2. Composition. The results of ICP-MS and ICP-OES analyses performed with 30.3 mg of AZP are compiled in Table 1. They showed a Zn:P ratio of 3.00:1.98 in good agreement with the composition $Zn_3(PO_4)_2 \times n\ H_2O$. EDX spectroscopy (Figure S1, Supporting Information) showed the presence of zinc, oxygen, and phosphorus without impurities from other precipitates. As the samples were coated with a thin layer sputtered carbon coating, a carbon signal appears in the spectrum as well. Semiquantitative analysis showed a Zn:P ratio of 3:2.

3.3. Structure. TEM snapshots of the product sampled after 5 s and prior to centrifugation (Figure 2C,D) showed noncrystalline species of coalesced nanoparticles crystallizing under strong electron radiation, reminiscent of liquid-like ACC particles obtained from related studies on $CaCO_3$.[81]

The nearly spherical nanoparticles had an average diameter of 22(2) nm and revealed a high degree of agglomeration, as can be seen in the SEM images (Figure 2A,B) of the product sampled after 5 s and centrifuged subsequently. These observation are supported by SAXS measurements (Figure S2, Supporting Information). The scattering curve of AZP shows no pronounced minima, indicating a high degree of aggregation (and/or polydispersity). By using the Kratky approximation an average diameter of the aggregates is determined to be 45 nm.

The featureless SAED pattern shown in the inset of Figure 2D supports the absence of long-range order in as-prepared zinc phosphate hydrate. Samples collected 4 min after rapid mixing of equal volumes of 15 mM $Zn(NO_3)_2$ and 10 mM

DOI: 10.1021/ja5103663
J. Am. Chem. Soc. 2015, 137, 2285−2294

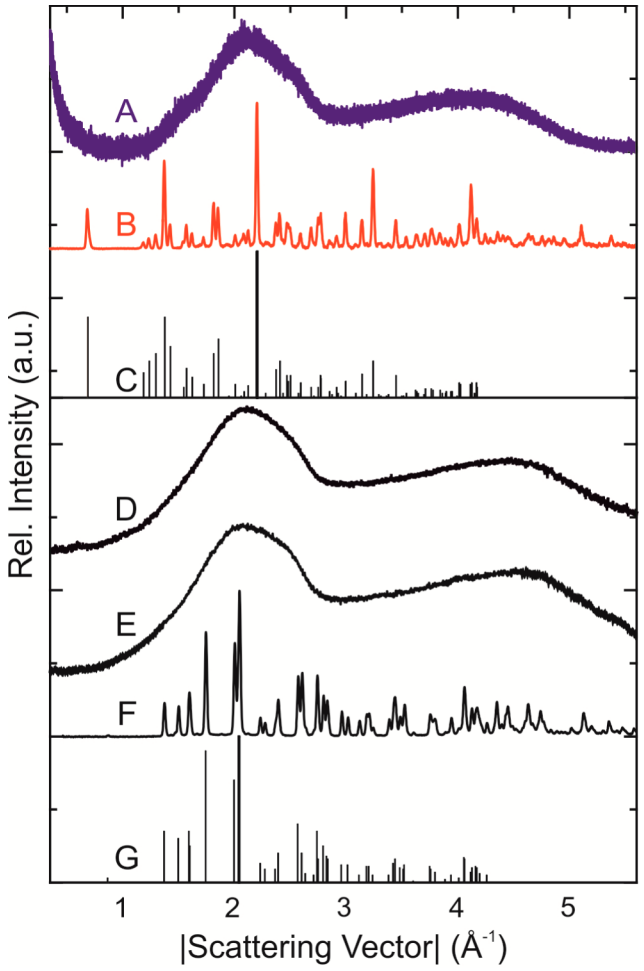

Figure 1. X-ray diffractograms of (A) amorphous zinc phosphate measured with high-energy synchrotron radiation and (B) hopeite. (C) Calculated line pattern of hopeite. (D and E) After heating A to 200 and 400 °C under argon for 1 week, the amorphous phase is still preserved. (F) At 600 °C only α-$Zn_3(PO_4)_2$, the thermodynamically stable phase at that temperature with (G) the calculated line pattern, was formed.

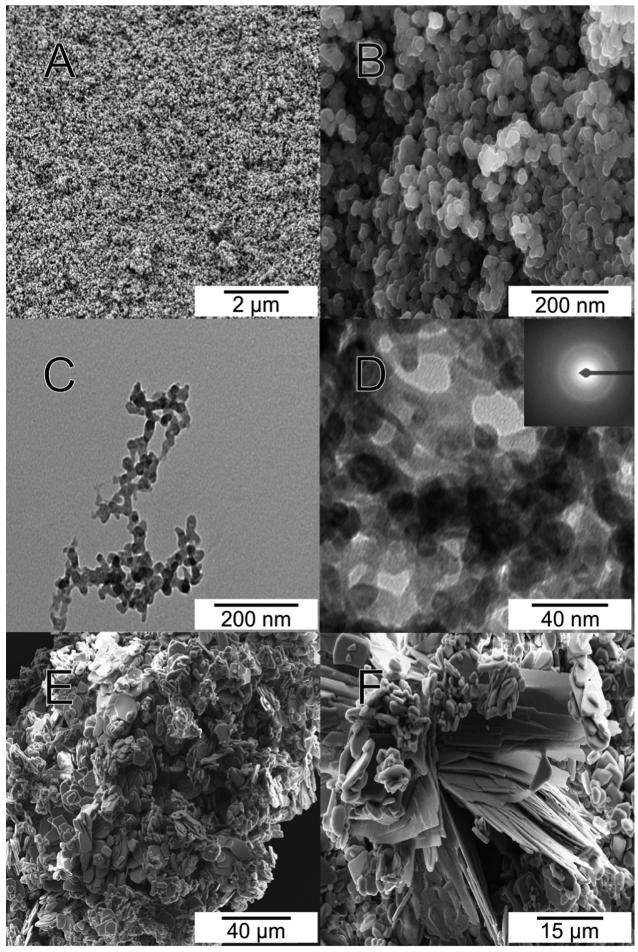

Figure 2. (A and B) SEM images of the precipitated AZP particles sampled 5 s after rapid mixing equal volumes of 15 mM $Zn(NO_3)_2$ and of 10 mM Na_3PO_4 solutions. (C and D) TEM images of AZP particles. The electron diffraction pattern shown in the inset of (D) is featureless, indicating the amorphous nature of the precipitate. (E and F) SEM images of hopeite sampled 4 min after rapid mixing equal volumes of 15 mM $Zn(NO_3)_2$ and of 10 mM Na_3PO_4 solutions.

Table 1. Results of the ICP-MS and ICP-OES Measurements[a]

ICP-MS	^{64}Zn	^{66}Zn	^{31}P
mean conc. (μg L^{-1})	131.1 ± 2.9	130.7 ± 3.4	41.3 ± 0.9
mean conc. (μmol L^{-1})	2.05 ± 0.05	1.98 ± 0.05	1.33 ± 0.03
ICP-OES	Zn		P
mean conc. (μg L^{-1})	132		41
mean conc. (μmol L^{-1})	2.02		1.32

[a]Mean concentrations (μg L^{-1}) and standard deviations for Zn and P in AZP; relative standard deviation of all the samples (RSD) are included.

Na_3PO_4 showed agglomerated plate-like crystals of hopeite (Figure 2E,F).

As vibrational spectroscopy provides direct access to the structure of the different phosphates, we measured the IR spectra normalized to the phosphate stretching mode of AZP (Figure 3, trace A) and hopeite (Figure 3, trace B) together with the spectra of the annealing products at 200, 400, and 600 °C under argon for 1 week (traces C–E). The two bottom traces show the Raman spectra of hopeite (trace G) and AZP (trace F). Signals observed in both IR and Raman spectra at 1000 cm^{-1} can be related to the stretching vibrations of the phosphate groups. The bands of free phosphate anions and water molecules are split due to factor group splitting and the lower site symmetry in the crystal structure of hopeite (traces B and G).[82] In AZP (traces A and F) no splitting occurs, and the bands ν_{as}(P–O) and δ_{as}(O–P–O) are broad but not split.

The water bands ν(O–H) and δ(H–O–H) become increasingly smaller in the spectra of the samples obtained at elevated temperatures (200, 400, and 600 °C) under argon. The nonsplit phosphate bands in traces D and E reveal that the samples are still amorphous, which can be seen by missing Bragg reflections in the corresponding XRD patterns as well (Figure 1D,E). The annealed phases (HT-AZP) contained less water than the AZP at room temperature (RT-AZP), as extracted from the calculated extinctions of the bands of the stretching and deformation modes of water ν(O–H) and δ(H–O–H) in the IR spectra (normalized to the PO_4^{3-} stretching mode, Table 2). According to the Beer–Lambert law the extinction of vibrations arising from water is proportional to the concentration of structural water within the sample.

DOI: 10.1021/ja5103663
J. Am. Chem. Soc. 2015, 137, 2285–2294

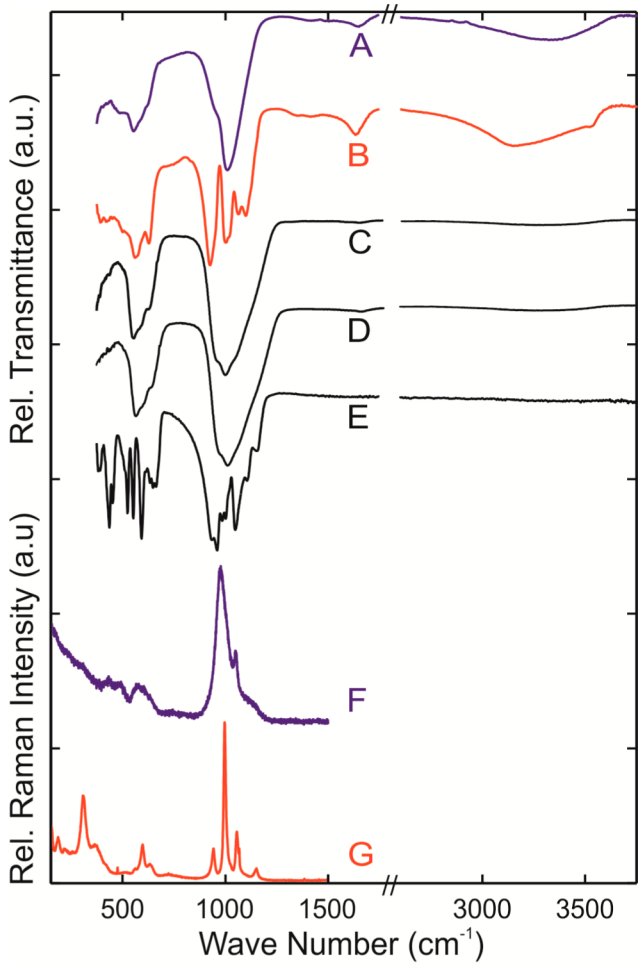

Figure 3. IR spectra normalized to the phosphate stretching mode of AZP (A) and hopeite (B). At 200 and 400 °C (under argon, for 1 week) AZP is still amorphous but contains less water (C and D). At 600 °C the thermodynamically stable phase at that temperature α-$Zn_3(PO_4)_2$ (E) exhibits a well-resolved band pattern. Raman spectra normalized to the phosphate stretching mode of hopeite (G) and AZP (F). The bands of hopeite and α-$Zn_3(PO_4)_2$ are split because of lattice symmetry constraints.

Table 2. Extinctions of the Water Bands in the Normalized IR Spectra of Different Zinc Phosphates and Resulting Water Content (Formula Units)

substance	$E(\nu(O-H))$ (a.u.)	water content	$E(\delta(H-O-H))$ (a.u.)	water content
hopeite	0.125	4.0	0.070	4.0
AZP	0.067	2.1	0.029	1.7
AZP, 200 °C	0.013	0.4	0.009	0.5
AZP, 400 °C	0.013	0.4	0.006	0.3
α-$Zn_3(PO_4)_2$	0.000	0.0	0.000	0.0

From the compositions for RT-AZP derived by IR spectroscopy ($Zn_3(PO_4)_2 \times 1.9\ H_2O$), thermal analysis (*vide infra*, $Zn_3(PO_4)_2 \times 2.5\ H_2O$), and ^{1}H MAS NMR spectroscopy (*vide infra*, $Zn_3(PO_4)_2 \times 1.7 \pm 0.2\ H_2O$), we assume an averaged value of $Zn_3(PO_4)_2 \times 2\ H_2O$. For the HT-AZP polymorph we deduced an averaged composition of $Zn_3(PO_4)_2 \times 0.5\ H_2O$ (IR spectroscopy showed: $Zn_3(PO_4)_2 \times 0.4\ H_2O$, thermal analysis *vide infra*: $Zn_3(PO_4)_2 \times 0.5\ H_2O$, ^{1}H MAS NMR spectroscopy *vide infra*: $Zn_3(PO_4)_2 \times 0.5\ H_2O$). At 600 °C the anhydrous crystalline polymorph α-$Zn_3(PO_4)_2$ was formed (trace E). The bands of the phosphate groups are split and well resolved in the IR spectrum. No water bands were observed.

The Raman spectra of AZP and hopeite (bottom traces) show more bands than the corresponding IR spectra because all normal modes of the phosphate anion are Raman active. However, bands of AZP (trace F) are broad and nonsplit, whereas the bands of hopeite (trace G) are split due to symmetry constraints in the crystalline structure.[83] For a complete listing of the vibration modes of the different phosphates see Table S1, Supporting Information.

3.4. Thermal Stability. The thermogravimetric and DSC traces of AZP under argon are displayed in Figure 4. A

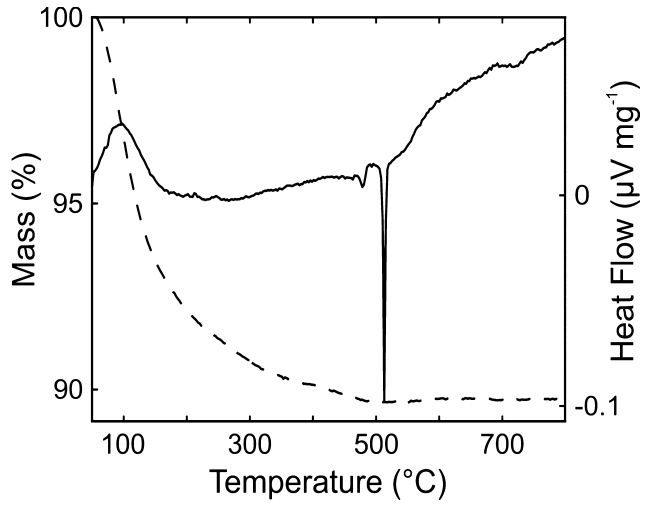

Figure 4. Thermogravimetric trace (dashed line) and DSC signal (full line) of AZP under argon.

continuous weight loss of 10.28% (accompanied by an endothermic DSC signal at 97 °C) occurred during heat-up, which is attributed to the loss of structural water because (i) no other volatile components are present and (ii) XRD and vibrational spectroscopy showed that at 600 °C only anhydrous α-$Zn_3(PO_4)_2$ is present. Surface bound water was removed prior to the heating step by drying the sample *in vacuo*. The weight loss lead to an approximate composition $Zn_3(PO_4)_2 \times 2.5\ H_2O$ in agreement with the IR spectroscopic results ($Zn_3(PO_4)_2 \times 1.9\ H_2O$), i.e., the amorphous phase contained less water than α-hopeite, the thermodynamically stable phase in this temperature range. Two exothermic signals in the DSC curve at 480 and 510 °C indicate a crystallization of AZP, where the anhydrous zinc phosphate α-$Zn_3(PO_4)_2$ is formed as demonstrated by XRD and IR spectroscopy (SEM image, Figure S3, Supporting Information).

AZP revealed a high thermal stability up to 480 °C; even annealing at 200 and 400 °C for 1 week under argon left the amorphous character unchanged (see Figure 1D,E). However, the annealing products (HT-AZP) at 200 and 400 °C contained less water than RT-AZP, which could be extracted from a quantitative analysis of the IR spectra (see Table 2) and derived by the weight loss observed in the thermal analysis (Table S2, Supporting Information). HT-AZP consists of coalesced spherical nanoparticles slightly bigger than RT-AZP (Figure S4, Supporting Information). The surprising stability of the amorphous nanoparticles can be explained either by very

DOI: 10.1021/ja5103663
J. Am. Chem. Soc. 2015, 137, 2285−2294

small volume diffusion coefficients in the solid state (kinetic barrier)[84] or by a crossover in thermodynamic stability at the nanoscale.[85] The presence of water during heat up in air leads to the formation of a mixture of zinc phosphate dihydrate, hopeite (which in fact contains more water than RT-AZP), and a large amount of amorphous phase at 200 °C. At 400 °C mixtures of α-$Zn_3(PO_4)_2$ and β-$Zn_3(PO_4)_2$ were obtained (Figure S5, Supporting Information). α-Hopeite has been reported to release its crystal water in three steps,[39] (Figure S6, Supporting Information), and β-hopeite is dehydrated via two metastable dehydration products, $Zn_3(PO_4)_2 \times 3\ H_2O$ and $Zn_3(PO_4)_2 \times H_2O$.[39]

As AZP contains less water than hopeite, we assume that the transformation from AZP to hopeite must occur in aqueous solution or requires at least atmospheric moisture or surface water as a mineralizer and crystal building block.[84] Crystalline hopeite was obtained even after very short reaction times (approximately 1 min) by resuspending (RT or HT)-AZP nanoparticles in water and separating them by centrifugation. In contrast, AZP transformed to hopeite in air after days. AZP is stable for months when stored under dry conditions. A possible reason for this behavior is the significantly lower activation energy for surface diffusion than for diffusion in the solid state.[84] As surface diffusion coefficients are nearly equivalent to those for diffusion in solution, adsorbed water leads to a high ion mobility of Zn^{2+} and PO_4^{3-} so that rearrangement and addition of water molecules lead to crystallization. Even a water film provided by atmospheric moisture may have this effect.[84]

3.5. Water Content and Mobility. The main goals of the solid-state NMR study were to (i) provide evidence of the amorphous structure of AZP, (ii) identify water of hydration and to quantify its amount, (iii) demonstrate that the transformation of AZP to hopeite is triggered by the uptake of atmospheric moisture, and (iv) study the stiffness of the hydrogen-bonding network which stabilizes AZP against crystallization.

The ^{31}P MAS NMR spectrum of AZP (Figure 5) displayed a broad signal, which is characteristic of amorphous materials but can also be obtained from small nanosized crystalline structures. Its chemical shift at ≈5 ppm is typical for zinc orthophosphates.[66,86] The same spectrum, taken after a few weeks, showed a similar broad signal of the amorphous phase and an additional sharp peak that was assigned to crystalline hopeite (Figure S7, Supporting Information).

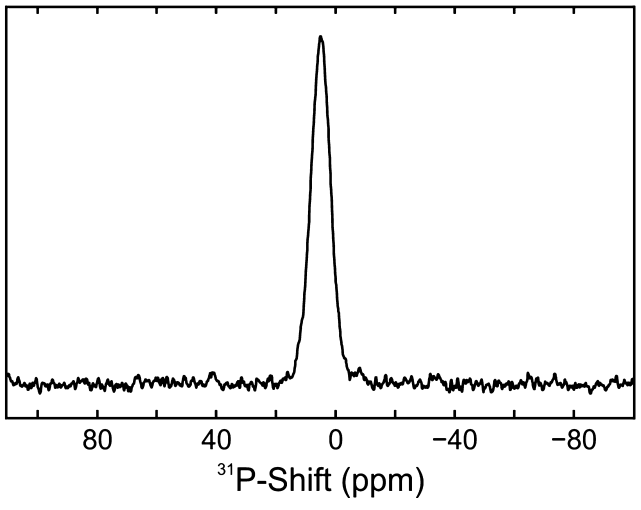

Figure 5. ^{31}P MAS NMR spectrum of AZP. Data were measured at ν_r = 40 kHz.

Unlike thermogravimetry, ^{1}H MAS NMR is able to differentiate between and quantify structural and surface water in AZP. The ^{1}H MAS NMR spectrum of AZP (Figure 6) showed mainly two peaks. One broad signal at 5.8 ppm (dashed line) was assigned to structural water, while a sharper peak at 5.5 ppm (dotted line) to mobile water adsorbed on the surface of the nanoparticles because of the absence of spinning side-bands observed for the peak assigned to mobile water. Both line shape and assignment were confirmed by ^{1}H{^{31}P} C-REDOR experiments (Figure S8, Supporting Information). These values are well within the range of chemical shifts reported for crystal water in inorganic materials.[86] The ^{1}H NMR quantification of the peak associated with structural water led to a composition $Zn_3(PO_4)_2 \times (1.7 \pm 0.2)\ H_2O$. The proton quantification of HT-AZP showed a composition with less structural water than RT-AZP (Figure S9, Supporting Information), which is in agreement with the results of IR spectroscopy and thermal analysis (Table S2, Supporting Information).

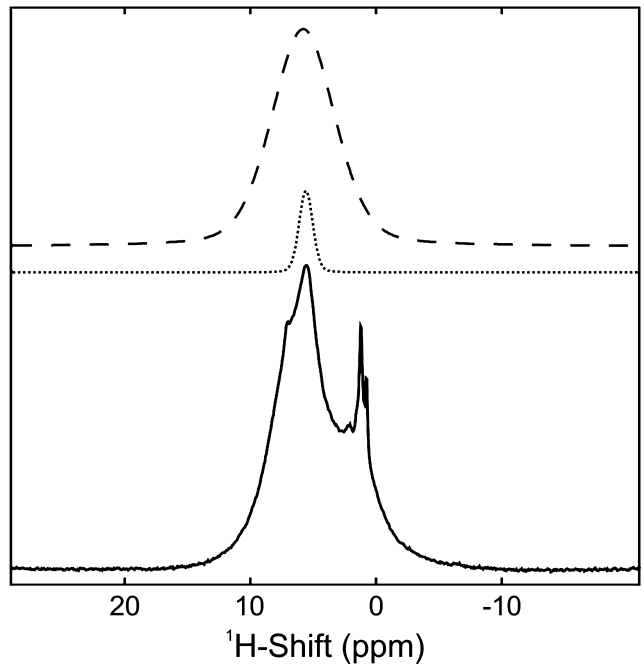

Figure 6. ^{1}H MAS NMR spectrum of AZP. Data were measured at ν_r = 40 kHz; broad peak (dashed line) was assigned to structural water, while the sharper peak (dotted line) to mobile water adsorbed on the surface of the nanoparticles (see main text); peaks at ≈1 ppm were assigned to acetone (used in the washing step) and the shoulder centered at ≈7 ppm to an unknown phase, while the peaks at 1 and 7 ppm do not contain P atoms according to the absence of dephasing observed in the ^{1}H{^{31}P} C-REDOR experiments (Figure S8, Supporting Information).

In order to corroborate the hypotheses that AZP is stabilized by a rigid hydrogen-bonding network and that it transforms to α-hopeite by absorbing atmospheric moisture, C-REDOR[69,70] experiments and a moment-based line shape analysis were performed. The curve of AZP (crosses in Figure 7) showed a slower dephasing toward the value $\Delta S/S_0 = 1$ than the curve of

DOI: 10.1021/ja5103663
J. Am. Chem. Soc. 2015, 137, 2285−2294

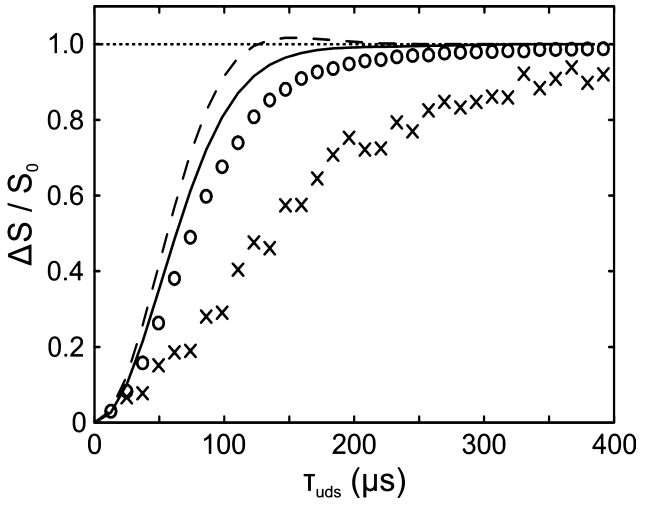

Figure 7. Experimental and simulated $^{31}P\{^{1}H\}$ C-REDOR curves. Experimental curve of the amorphous component (crosses) and crystalline α-hopeite (circles). Simulated curve for α-hopeite: static model (dashed line) and one under consideration of the two-site jump between hydrogen atoms in structural water molecules (solid line). Data were measured at ν_r = 40 kHz.

α-hopeite (circles). Simulations helped to understand these results, which we will discuss in the following.

C-REDOR is one flavor of the prominent REDOR[87] experiment. Both are used to determine internuclear distance constraints and study spatial proximities between NMR-active nuclei.[88] In the case of a multispin system the use of C-REDOR is more advantageous, since it is able to suppress to first-order average Hamiltonian theory[89] unwanted homonuclear dipole−dipole interactions.[69,70] Analytical expressions for the investigation of multispin systems have been derived for the REDOR[90,91] experiment and adapted to C-REDOR (eqs 1 and 2).[92] The symbols used in eqs 1 and 2 are explained in Section S1, Supporting Information. Based on this knowledge it is possible to predict accurate C-REDOR curves of a crystal up to full dephasing with a home-written Fortran90 program, which can handle the interactions between thousands of spins. It turns out that the simulation converges for spin systems with around 80 spins or more, where the atomic positions can be retrieved from crystallographic data.

$$\left\langle \frac{S_D}{S_0} \right\rangle = \langle \prod_{n}^{k=1} \cos[\sqrt{2/3}\,\pi|\kappa|\nu_{dip,k}\tau\varepsilon_k] \rangle \quad (1)$$

$$\nu_{dip,k} = -\frac{\mu_0\gamma_I\gamma_S\hbar}{8\pi^2 r_k^3} \quad (2)$$

The dashed line in Figure 7 displays the analytically calculated $^{31}P\{^{1}H\}$ C-REDOR curve of α-hopeite based on eq 1 using the universal dephasing scale τ_{uds}.[66] A better agreement between experimental and simulated data is achieved after incorporating a two-site jump process between the two hydrogen atoms in a water molecule into the calculation (solid line) according to eq 3.[92]

$$\left\langle \frac{S_D}{S_0} \right\rangle = \left\langle \prod_{n}^{k=1} \cos\left[\sum_{N}^{j=1} p_{eq}(j)[\sqrt{2/3}\,\pi|\kappa|\nu_{dip,k}\tau\varepsilon_k] \right] \right\rangle \quad (3)$$

In this model, the two hydrogen atoms of the water molecule switch places infinitely fast as in an N-stepped jump process. The difference between eqs 1 and 3 is in the cosine's argument that is now the weighted sum of the N possible positions of the kth spin, in this case one of the hydrogen atoms. The weighting factor is given by the probability $p_{eq}(j)$ of finding an atom in a certain position, where $\sum_{j=1}^{N} p_{eq}(j) = 1$. Clearly, the experimental curve for α-hopeite can be described neither by a static spin-system nor by a completely mobile arrangement of H atoms. The truth is somewhere in between. We attribute the deviations between experiment and simulation to random local motional processes like the shown two-site jump.

The $^{31}P\{^{1}H\}$ C-REDOR curve of AZP slower dephases than that of α-hopeite (Figure 7 and Figure S10, Supporting Information). This translates to a lower value of the so called effective dipole dipole constant.[93] In principle this can be explained by a lower water content, longer $^{31}P-^{1}H$ distances, dynamics, or a combination thereof. Since AZP is amorphous, the prediction of its $^{31}P\{^{1}H\}$ C-REDOR curve is not trivial. Taking α-hopeite as a model for AZP the lower content of H atoms in form of structural water offers a simple explanation for the slower dephasing of the respective REDOR curves. We took the structure of α-hopeite with only half of the amount of structural water as a model for AZP and predicted the average static C-REDOR curve and the average one accounting for two-site jumps (Figure S10, Supporting Information). We conclude that the REDOR experiments give evidence for hydrogen-bonding network where local H-motions are partially activated and lead to less efficient dephasing than that of a rigid hydrogen-bonding network.

In the following we will analyze the second moment of the static ^{1}H NMR spectra of AZP and α-hopeite as a second tool to study the stiffness of the hydrogen-bonding network. Second moments of the line shape are sensitive to dynamics in solids and can be calculated according to the Van Vleck formula (symbols are explained in the Supporting Information):[94,95]

$$M_2^{II} = \frac{3}{5}\left(\frac{\mu_0}{4\pi}\right)^2 \gamma^4\hbar^2 I(I+1)\frac{1}{N}\sum_{i\neq j}^{N}\frac{1}{r_{ij}^6} \quad (4)$$

In eq 4 M_2 is given in angular frequency. Based on crystallographic data, we calculated the square roots of the second moments $(M_{2,calc}^{II})^{1/2}/(2\pi)$ of gypsum[96] ($CaSO_4 \times 2\ H_2O$), chalcanthite[97] ($CuSO_4 \times 5\ H_2O$), and α-hopeite as rigid structures (Table 3).

Table 3. Square Roots of Second Moments $(M_2)^{1/2}/(2\pi)$ of Hydrates Calculated for Rigid Structures and a Few of the Shortest H−H Distances

substance	$(M_{2,calc}^{II})^{1/2}/(2\pi)$ (kHz)	r_{HH} (Å)
$CaSO_4 \times 2\ H_2O$[a]	24.4[a,c]	1.533
$CuSO_4 \times 5\ H_2O$[a]	23.9[a,c]	1.552/1.540/1.567/1.600
$Zn_3(PO_4)_2 \times 4\ H_2O$[b]	33.9[b,c]/40.0[d]	1.249/1.315/1.853

[a]Neutron diffraction data. [b]XRD data. [c]Calculated value according to eq 4. [d]Experimental value, this work.

For a single structural water molecule in gypsum eq 4 features $(M_{2,calc}^{II})^{1/2}/(2\pi)$ = 22.4 kHz. Comparing this value to the case of some hydrated minerals (Table 3), it becomes clear that the value of the intramolecular interaction is already close to the value calculated for a whole crystal structure. For this reason, many other hydrates (not shown) feature a value $(M_{2,calc}^{II})^{1/2}/(2\pi)$ in this range. Here it should be noted, that the

DOI: 10.1021/ja5103663
J. Am. Chem. Soc. 2015, 137, 2285−2294

observable experimental values at room temperature and even at lower ones are often a lot smaller due to the dynamics of structural water.[98−100]

The experimental value of $(M^{II}_{2,exp})^{1/2}/(2\pi)$ = 40.0 kHz for α-hopeite (spectrum not shown) is therefore very large. The calculated value is also large, although the best crystal structure we found for calculation was solved by XRD, which leads to controversial hydrogen positions. Taking into account contributions from heteronuclear interactions (≈1 kHz), ^{1}H chemical shift anisotropy (up to ≈4.3 kHz), and transverse relaxation (≈1 kHz), we conclude that the motion in α-hopeite can be described as a two-site jump which does not reduce the main contribution[101] to the second moment and explains both the observed C-REDOR curve and the static ^{1}H line shape.

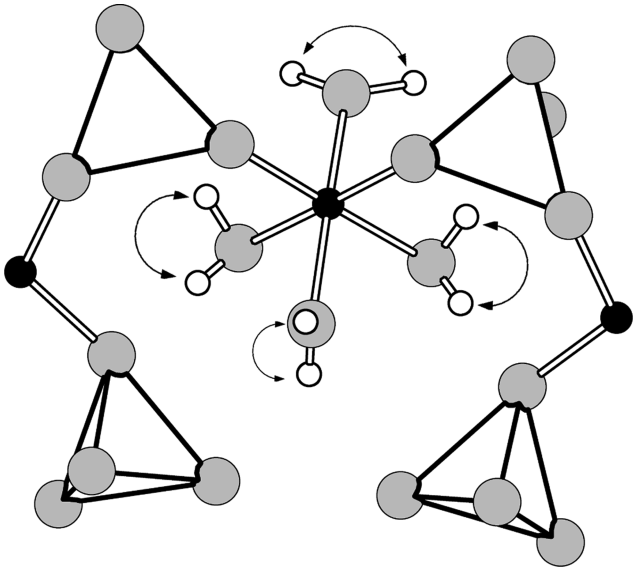

Figure 8. Excerpt from the crystal structure of hopeite, showing the two-site jump process between the two hydrogen atoms of crystal water molecules, which was taken into account to simulate the ^{31}P{^{1}H} C-REDOR curve (gray spheres, O; empty spheres, H; black spheres, Zn atoms; P atoms are located in the center of the tetrahedron formed by the O atoms).

The experimental value of $(M^{II}_{2,exp})^{1/2}/(2\pi)$ = 17 kHz for RT-AZP was estimated from a ^{1}H spin−echo spectrum of a static sample (Figure S11, Supporting Information) while neglecting the contribution from the distribution of chemical shifts in a noncrystalline sample. This value is already close to the calculated ones for other hydrates, which represent models featuring rigid structural water molecules (Table 3). In fact, such experimental values are often only achieved at lower temperatures. Thus, structural water in AZP seems to show only little dynamics at room temperature as compared to other hydrates. Thus, the observations made in the NMR experiment indicate a stiff hydrogen-bonding network, which explains that AZP is relatively stable against crystallization.

4. CONCLUSIONS

Zinc phosphate is an attractive example for examining fundamental processes of crystallization. (i) It is polymorphous, and we were able to synthesize (ii) amorphous zinc phosphate hydrate nanoparticles (AZP) with diameters of ≈20 nm by direct precipitation from aqueous solutions of Zn^{2+} and PO_4^{3-} at low concentrations and short reaction times (subsequent annealing results in a high-temperature phase). (iii) Zinc phosphates are structurally still simple enough to serve as model compounds for a fundamental understanding of nucleation and crystallization processes from aqueous solution.

The synthesis of the AZP nanoparticles supports the hypothesis that the formation of the metastable over the thermodynamically stable polymorph (with higher lattice energy) is favored because of surface energy. The precipitation must be fast in order to avoid the precipitation of $Zn(OH)_2$ (K_L = 3.0 × 10^{-17} mol^{-3}) which is formed in a competing reaction even at neutral pH. Furthermore, the separation of AZP must be fast enough to avoid the transformation to hopeite via dissolution−recrystallization. This could be demonstrated by resuspending AZP nanoparticles in water and monitoring their transformation to hopeite.

In agreement with thermoanalytical results, hydrogen quantification using ^{1}H solid-state NMR and heteronuclear dipolar recoupling experiment (C-REDOR) showed lower water content in AZP than in α-hopeite. Simulations of C-REDOR curves and a second moment analysis indicated dynamics in α-hopeite and AZP to be described as an infinitely fast two-site jump process, with an otherwise rather rigid structural water network.

AZP was characterized by electron microscopy, XRD and SAXS, vibrational, MAS NMR spectroscopy, and thermal analysis. It is extraordinarily stable in the absence of water. Annealing RT-AZP with the approximate composition $Zn_3(PO_4)_2$ × 2 H_2O at 400 °C resulted in the formation of HT-AZP with lower water content ($Zn_3(PO_4)_2$ × 0.5 H_2O). Anhydrous α-$Zn_3(PO_4)_2$ was formed at 600 °C by release of structural water. The "water-deficient" amorphous phase may provide a starting point for further structural investigations. However, it would not be accurate to say that zinc phosphate shows polyamorphism because RT-AZP and HT-AZP differ in their water content and therefore do not have the same composition.[102−104]

What is the reason for the thermal stability of AZP with respect to hopeite? First, hopeite ($Zn_3(PO_4)_2$ × 4 H_2O), the thermodynamically stable crystalline polymorph, contains more structural water than the AZP. In addition, the transformation from the amorphous to the crystalline phase may occur (i) via dissolution and recrystallization or (ii) as a direct solid−solid transformation. During the crystallization of AZP water serves as a mineralizer that facilitates the transport of the insoluble "nutrient" to a seed crystal, i.e., it acts as catalysts for crystallization by enhancing the mobility of the ionic constituents.[105] Upon heating in the absence of water this process is blocked, and AZP is stabilized kinetically. We assume that a variety of other systems exist where amorphous polymorphs play an important role as crystallization intermediates. Good indicators should be (i) the cation charge density, which makes the hydration enthalpy comparable to the binding energy of the counter-anions. (ii) Anions whose acidities allow the formation of hydrogen-bonded networks may favor multistage crystallization processes involving the homogeneous precipitation of nanocrystalline hydrated phases, and an assembly of aggregates by condensation/dehydration with subsequent transformation into thermodynamically stable end products. The moderate charge densities of Zn^{2+} and PO_4^{3-} allow the formation of hydrogen-bonded networks in hydrated polymorphs zinc phosphate.

DOI: 10.1021/ja5103663
J. Am. Chem. Soc. 2015, 137, 2285−2294

■ ASSOCIATED CONTENT

Supporting Information

EDX spectrum of RT-AZP (Figure S1); SAXS data of RT-AZP (Figure S2); SEM image of α-$Zn_3(PO_4)_2$ (Figure S3); TEM image of HT-AZP (Figure S4); X-ray diffractograms of RT-AZP annealed in air (Figure S5); DSC/TGA of hopeite (Figure S6); ^{31}P MAS NMR spectrum of RT-AZP after 4 weeks (Figure S7); $^{1}H\{^{31}P\}$ C-REDOR curve of RT-AZP (Figure S8); ^{1}H MAS NMR spectra of HT-AZP (Figure S9); experimental and simulated $^{31}P\{^{1}H\}$ C-REDOR curves—model half amount of water (Figure S10); static ^{1}H spin—echo NMR spectrum of RT-AZP (Figure S11); results of IR and Raman spectroscopy in detail (Table S1); TGA data of HT-AZP (Table S2); explanation of symbols used in eqs 1, 2, and 4 (Section S1). This material is available free of charge via the Internet at http://pubs.acs.org.

■ AUTHOR INFORMATION

Corresponding Author

*tremel@uni-mainz.de

Notes

The authors declare no competing financial interest.

■ ACKNOWLEDGMENTS

This study was funded by the Deutsche Forschungsgemeinschaft (DFG) within the priority program 1415. S.B. is recipient of a VCI Fellowship and a collegiate of the MAINZ Graduate School of the State of Rhineland-Palatinate. We also thank R. Jung-Pothmann for X-ray diffraction measurements. The microscopy equipment is operated by the Electron Microscopy Center Mainz (EMZM), supported by the Johannes Gutenberg University and the Max Planck Institute for Polymer Research (MPI-P). We thank Prof. W. Hofmeister and Prof. S. Waldvogel for access to the Raman and IR spectrometers, C. Minke for technical assistance with the NMR spectrometer, and Prof. W. Schnick for access to the NMR spectrometer.

■ REFERENCES

(1) Myerson, A. S. *Handbook of Industrial Crystallization*, 2nd ed.; Butterworth-Heinemann: Woburn, MA, 2001.
(2) *Kristallisation in der industriellen Praxis*; Hofmann, G., Ed.; Wiley-VCH: Weinheim, Germany, 2004.
(3) Kleber, W.; Bautsch, H. J.; Bohm, H.; Klimm, D. *Einführung in die Kristallographie*; Verlag Technik GmbH: Berlin, Germany, 2002.
(4) Kelton, K. F.; Greer, A. *Nucleation in Condensed Matter Applications in Materials and Biology*; Pergamon: Oxford, U.K., 2010; p 15.
(5) Morse, J. W.; Arvidson, R. S.; Lüttge, A. *Chem. Rev.* **2007**, *107*, 342—381.
(6) Addadi, L.; Raz, S.; Weiner, S. *Adv. Mater.* **2003**, *15*, 959—970.
(7) Politi, Y.; Levi-Kalisman, Y.; Raz, S.; Wilt, F.; Addadi, L.; Weiner, S.; Sagi, I. *Adv. Funct. Mater.* **2006**, *16*, 1289—1298.
(8) Politi, Y.; Metzler, R. A.; Abrecht, M.; Gilbert, B.; Wilt, F. H.; Sagi, I.; Addadi, L.; Weiner, S.; Gilbert, P. U. P. A. *Proc. Natl. Acad. Sci. .U.S.A.* **2008**, *105*, 17362—17366.
(9) Brecevic, L.; Nielsen, A. E. *J. Cryst. Growth* **1989**, *98*, 504—510.
(10) Faatz, M.; Gröhn, F.; Wegner, G. *Adv. Mater.* **2004**, *16*, 996—1000.
(11) Lam, R. S. K.; Charnock, J. M.; Lennie, A.; Meldrum, F. C. *CrystEngComm* **2007**, *9*, 1226—1236.
(12) Gower, L. B.; Odom, D. J. *J. Cryst. Growth* **2000**, *210*, 719—734.
(13) Wang, D.; Wallace, A. F.; De Yoreo, J. J.; Dove, P. M. *Proc. Natl. Acad. Sci. U.S.A.* **2009**, *106*, 21511—21516.
(14) Donners, J. J. J. M.; Heywood, B. R.; Meijer, E. W.; Nolte, R. J. M.; Roman, C.; Schennin, A. P. H. J.; Sommerdijk, N. A. J. M. *Chem. Commun.* **2000**, 1937—1938.
(15) Li, M.; Mann, S. *Adv. Funct. Mater.* **2002**, *12*, 773—779.
(16) Gebauer, D.; Voelkel, A.; Coelfen, H. *Science* **2008**, *322*, 1819—1822.
(17) Pouget, E. M.; Bomans, P. H. H.; Goos, J. A. C. M.; Frederik, P. M.; de With, G.; Sommerdijk, N. A. J. M. *Science* **2009**, *323*, 1455—1458.
(18) Natalio, F.; Coralles, T.; Panthöfer, M.; Lieberwirth, I.; Schollmeyer, D.; Müller, W. E. G.; Kappl, M.; Butt, H.-J.; Tremel, W. *Science* **2013**, *339*, 1298—1302.
(19) DeYoreo, J. J.; Zepeda-Ruiz, L. A.; Friddle, R. W.; Qiu, S. R.; Wasylenski, L. E.; Chernov, A. A.; Gilmer, G. H.; Dove, P. M. *Cryst. Growth Des.* **2009**, *9*, 5135—5144.
(20) Gebauer, D.; Gunawidjaja, P. N.; Ko, J. Y. P.; Bacsik, Z.; Aziz, B.; Liu, L.; Hu, Y.; Bergström, L.; Tai, C.-W.; Sham, T.-K.; Eden, M.; Hedin, N. *Angew, Chem. Int. Ed.* **2010**, *49*, 8889—8891.
(21) Wolf, S. E.; Müller, L.; Barrea, R.; Leiterer, J.; Panne, U.; Hoffmann, T.; Emmerling, A. F.; Tremel, W. *Nanoscale* **2011**, *3*, 1158—1165.
(22) Volmer, M.; Weber, A. *Z. Phys. Chem.* **1925**, *119*, 277—301.
(23) Dey, A.; Bomans, P. H.; Müller, F. A.; Will, J.; Frederik, P. M.; de With, G.; Sommerdijk, N. A. *Nat. Mater.* **2010**, *9*, 1010—1014.
(24) van Driessche, A. E. S.; Benning, L. G.; Rodriguez-Blanco, J. D.; Ossorio, M.; Bots, P.; Garcia-Ruiz, J. M. *Science* **2012**, *336*, 69—72.
(25) Weiss, H.; Bräu, M. F. *Angew. Chem., Int. Ed.* **2009**, *48*, 3520—3524.
(26) Arnaud, Y.; Sahakian, E.; Romand, M.; Charbonnier, J. C. *Appl. Surf. Sci.* **1988**, *32*, 281—295.
(27) Gardner, P. J.; McArn, I. W.; Bartob, V.; Seydt, G. M. *Surf. Coat. Int.* **1990**, *74*, 16—17.
(28) Haussühl, S.; Middendorf, B.; Dörfel, M. *J. Solid State Chem.* **1991**, *93*, 9—16.
(29) Pawlig, O.; Trettin, R. *Mater. Res. Bull.* **1999**, *34*, 1959—1966.
(30) Del Amo, B.; Romagnoli, R.; Vetere, V. F.; Hernandez, L. S. *Progr. Org. Coat.* **1998**, *33*, 28—35.
(31) Herschke, L.; Enkelmann, V.; Lieberwirth, I.; Wegner, G. *Chem.—Eur. J.* **2004**, *10*, 2795—2803.
(32) Liebau, F. *Acta Crystallogr.* **1965**, *18*, 352—354.
(33) Calvo, C. *Can. J. Chem.* **1965**, *43*, 436—445.
(34) Whitaker, A. *Acta Crystallogr.* **1975**, *B31*, 2026—2035.
(35) Hill, R. J.; Jones, J. B. *Am. Mineral.* **1976**, *61*, 987—995.
(36) *NBS Monogr. (U. S.)* **1979**, *25* (16), 80.
(37) *NBS Monogr. (U. S.)* **1979**, *25* (16), 81.
(38) *NBS Monogr. (U. S.)* **1979**, *25* (16), 83.
(39) Yuan, A.-Q.; Wu, J.; Huang, Z.-Y.; Zhou, Z.-G.; Wen, Y. X.; Tong, Z.-F. *Chin. J. Chem.* **2007**, *25*, 857—862.
(40) Gier, T. E.; Stucky, G. D. *Nature* **1991**, *349*, 508—510.
(41) Liu, W.; Liu, Y.; Shi, Z.; Pang, W. *J. Mater. Chem.* **2000**, *10*, 451—455.
(42) Cheetham, A. K.; Ferey, G.; Loiseau, T. *Angew. Chem., Int. Ed.* **1999**, *38*, 3268—3292.
(43) Oliver, S.; Kuperman, A.; Ozin, G. A. *Angew. Chem., Int. Ed.* **1998**, *37*, 46—62.
(44) Li, J.; Yu, J.; Yan, W.; Xu, Y.; Xu, W.; Qiu, S.; Xu, R. *Chem. Mater.* **1999**, *11*, 2600—2606.
(45) Bohlsen, F.; Kern, M. *Quintessence Int.* **2003**, *34*, 493—496.
(46) Squier, R. S.; Agar, J. R.; Duncan, J. P.; Taylor, T. D. *Int. J. Oral Maxillofac Implants* **2001**, *16*, 793—798.
(47) Milutinovic-Nikolic, A. D.; Medic, V. B.; Vukovic, Z. M. *Dental Mater.* **2007**, *23*, 674—678.
(48) Day, R. M.; Boccaccini, A. R. *J. Biomed. Mater. Res., Part A* **2005**, *73*, 73—79.
(49) Pawlig, O.; Trettin, R. *Chem. . Mater.* **2000**, *12*, 1279—1287.
(50) Meyer, G. *Farbe Lack* **1963**, *69*, 528—532.
(51) Meyer, G. *Farbe Lack* **1965**, *71*, 113—119.
(52) Clay, M. F.; Cox, G. H. *J. Oil Colour Chem. Assoc.* **1973**, *56*, 13—16.

DOI: 10.1021/ja5103663
J. Am. Chem. Soc. 2015, 137, 2285—2294

(53) Yoshihara, T.; Okita, H. *Trans. Iron Steel Inst. Jpn.* **1983**, *23*, 984−993.
(54) Adrian, G.; Bittner, A. *J. Coat. Technol.* **1986**, *58*, 59−65.
(55) Romagnoli, R.; Vetere, V. F. *Corrosion* **1995**, *51*, 216−223.
(56) Sankara Narayanan, T. S. N. *Rev. Adv. Mater. Sci.* **2005**, *9*, 130−177.
(57) Calvo, C. *J. Phys. Chem. Solids* **1963**, *24*, 141−149.
(58) Berkowitz, J. K.; Olsen, J. A. *J. Lumin.* **1991**, *50*, 111−115.
(59) Wang, J.; Wang, S.; Su, Q. *J. Mater. Chem.* **2004**, *14*, 2569−2574.
(60) Navrotsky, A.; Mazeina, L.; Majzlan, L. *Science* **2008**, *319*, 1635−1638.
(61) McHale, J. M.; Auroux, A.; Perrotta, A. J.; Navrotsky, A. *Science* **1997**, *277*, 788−791.
(62) Navrotsky, A. *Geochem. Trans.* **2003**, *4*, 34−37.
(63) Radha, A. V.; Forbes, T. Z.; Killian, C. E.; Gilbert, P. U. P. A.; Navrotsky, A. *Proc. Natl. Acad. Sci. U.S.A.* **2010**, *107*, 16438−16443.
(64) Yuan, A. Q.; Liao, S.; Tong, Z. F.; Wu, J.; Huang, Z. Y. *Mater. Lett.* **2006**, *60*, 2110−2114.
(65) Smith, A. L. *J. Electrochem. Soc.* **1951**, *98*, 363−368.
(66) Roming, M.; Feldmann, C.; Avadhut, Y. S.; Schmedt auf der Günne, J. *Chem. Mater.* **2008**, *20*, 5787−5795.
(67) Avadhut, Y. S.; Weber, J.; Hammarberg, E.; Feldmann, C.; Schellenberg, I.; Pöttgen, R.; Schmedt auf der Günne, J. *Chem. Mater.* **2011**, *23*, 1526−1538.
(68) Avadhut, Y. S.; Schneider, D.; Schmedt auf der Günne, J. *J. Magn. Reson.* **2009**, *201*, 1−6.
(69) Chan, J. C. C.; Eckert, H. J. *Chem. Phys.* **2001**, *115*, 6095−6105.
(70) Chan, J. C. C. *Chem. Phys. Lett.* **2001**, *335*, 289−297.
(71) Harris, R. K.; Becker, E. D.; Cabral de Menezes, S. M.; Granger, P.; Hoffman, R. E.; Zilm, K. W. *Pure Appl. Chem.* **2008**, *80*, 59−84.
(72) Herschke, L.; Rottstegge, J.; Lieberwirth, I.; Wegner, G. *J. Mater. Sci.: Mater. Med.* **2006**, *17*, 81−94.
(73) Wang, J.; Toby, B. H.; Lee, L. P.; Ribaud, L.; Antao, S.; Kurtz, C.; Ramanathan, M.; von Dreele, R. B.; Beno, M. A. *Rev. Sci. Instrum.* **2008**, *79*, 085105.
(74) Lee, P. L.; Shu, D.; Ramanathan, M.; Preissner, C.; Wang, J.; Beno, M. A.; von Dreele, R. B.; Ribaud, L.; Kurtz, C.; Antao, S. M.; Jiao, X.; Toby, B. H. *J. Synchr. Rad.* **2008**, *15*, 427−432.
(75) Dalesio, L. R.; Hill, J. O.; Kraimer, M.; Lewis, S.; Murray, D.; Hunt, S.; Watson, W.; Clausen, M.; Dalesio, J. *Nucl. Instrum. Methods Phys. Res., Sect. A* **1994**, *352*, 179−184.
(76) Reichle, R. A.; McCurdy, K. G.; Hepler, L. G. *Can. J. Chem.* **1975**, *53*, 3841−3845.
(77) Ostwald, W. *Z. Phys. Chem.* **1897**, *22*, 289−330.
(78) Cölfen, H.; Antonietti, M. *Mesocrystals and Non-Classical Crystallization*; Wiley-VCH: Weinheim, Germany, 2008.
(79) Herschke, L. Polymer controlled mineralization of zinc phosphate hydrates and applications in Corrosion Protection, Catalysis and Biomedicine. Ph.D. Thesis, Mainz, June 2004.
(80) Lewis, A. E.; Mangere, M. *Chem. Eng. Technol.* **2011**, *34*, 517−524.
(81) Wolf, S. E.; Leiterer, J.; Emmerling, F.; Tremel, W. *J. Am. Chem. Soc.* **2008**, *130*, 12342−12347.
(82) Cartwright, J. H. E.; Checa, A. G.; Gale, J. D.; Gebauer, G.; Sainz-Diaz, C. I. *Angew. Chem., Int. Ed.* **2012**, *51*, 11960−11970.
(83) Mangalam, G.; Das, S. J. *Arch. Phys. Res.* **2010**, *1*, 54−61.
(84) Schäfer, H. *Angew. Chem.* **1971**, *83*, 35−42.
(85) Navrotsky, A. *Proc. Natl. Acad. Sci. U.S.A.* **2004**, *101*, 12096−12101.
(86) MacKenzie, K. J. D.; Smith, M. E. *Multinuclear Solid-State Nuclear Magnetic Resonance of Inorganic Materials*; Elsevier Science, Ltd.: Oxford, U.K., 2002.
(87) Gullion, T.; Schaefer, J. *J. Magn. Reson.* **1989**, *81*, 196−200.
(88) Saalwächter, K.; Spiess, H. W. *J. Chem. Phys.* **2012**, *114*, 5707−5728.
(89) Haeberlen, U.; Waugh, J. S. *Phys. Rev.* **1968**, *175*, 453−467.
(90) Brouwer, E. B.; Gougeon, R. D. M.; Hirschinger, J.; Udachin, K. A.; Harris, R. K.; Ripmeester, J. A. *Phys. Chem. Chem. Phys.* **1999**, *1*, 4043−4050.
(91) Goetz, J. M.; Schaefer, J. *J. Magn. Reson.* **1997**, *127*, 147−154.
(92) Celinski, V. R.; Weber, J.; Schmedt auf der Günne, J. *Solid State Nucl. Magn. Reson.* **2013**, *49*−*50*, 12−22.
(93) Schmedt auf der Günne, J. *J. Magn. Reson.* **2003**, *165*, 18−32.
(94) Van Vleck, J. H. *Phys. Rev.* **1948**, *74*, 1168−1183.
(95) Brunner, E.; Sternberg, U. *Prog. Nucl. Magn. Reson. Spectrosc.* **1998**, *32*, 21−57.
(96) Pedersen, B. F.; Semmingsen, D. *Acta Crystallogr.* **1982**, *B38*, 1074−1077.
(97) Bacon, G. E.; Curry, N. A. *Proc. R. Soc. A* **1962**, *266*, 95−108.
(98) Mikuli, E.; Grad, B.; Medycki, W.; Hołderna-Natkaniec, K. *J. Solid State Chem.* **2004**, *177*, 3795−3804.
(99) Holcomb, D. F.; Pedersen, B. *J. Chem. Phys.* **1962**, *36*, 3270−3278.
(100) Pake, G. E. *J. Chem. Phys.* **1948**, *16*, 327−336.
(101) Migdał-Mikuli, A.; Mikuli, E.; Hetmańczyk, J.; Hetmańczyk, Ł.; Hołderna-Natkaniec, K.; Natkaniec, I. *J. Alloys Compd.* **2009**, *469*, 73−81.
(102) Mishima, O.; Stanley, E. *Nature* **1998**, *396*, 329−335.
(103) Smith, K. H.; Shero, E.; Chizmeshya, A.; Wolf, G. H. *J. Chem. Phys.* **1995**, *102*, 6851−6857.
(104) Poole, P. H.; Grande, T.; Sciortino, F.; Stanley, H. E.; Angell, C. A. *Comput. Mater. Sci.* **1995**, *4*, 373−382.
(105) Gnielinski, V.; Mersmann, A.; Thurner, F. *Verdampfung, Kristallisation, Trocknung*; Springer: Germany, 1993.

DOI: 10.1021/ja5103663
J. Am. Chem. Soc. 2015, 137, 2285−2294